Journal of MATERIALS RESEARCH

Article
DOI: 10.1557/jmr.2019.150

Optimized ALD-derived MgO coating layers enhancing silicon anode performance for lithium ion batteries

Xia Tai[1], Xifei Li[2,a)], Alibek Kakimov[3], Shiyu Li[3], Wen Liu[3], Jianwei Li[3], Jie Xu[1], Dejun Li[1], Xueliang Sun[4]

[1]Tianjin International Joint Research Centre of Surface Technology for Energy Storage Materials, College of Physics and Materials Science, Tianjin Normal University, Tianjin 300387, China
[2]Tianjin International Joint Research Centre of Surface Technology for Energy Storage Materials, College of Physics and Materials Science, Tianjin Normal University, Tianjin 300387, China; and Institute of Advanced Electrochemical Energy & School of Materials Science and Engineering, Xi'an University of Technology, Xi'an, Shaanxi 710048, China
[3]Institute of Advanced Electrochemical Energy & School of Materials Science and Engineering, Xi'an University of Technology, Xi'an, Shaanxi 710048, China
[4]Tianjin International Joint Research Centre of Surface Technology for Energy Storage Materials, College of Physics and Materials Science, Tianjin Normal University, Tianjin 300387, China; Institute of Advanced Electrochemical Energy & School of Materials Science and Engineering, Xi'an University of Technology, Xi'an, Shaanxi 710048, China; and Nanomaterials and Energy Lab, Department of Mechanical and Materials Engineering, Western University London, Ontario N6A 5B9, Canada
[a)]Address all correspondence to this author. e-mail: xfli2011@hotmail.com

Received: 10 February 2019; accepted: 8 April 2019

In this work, atomic layer deposition (ALD), as a novel strategy, has been applied to deposit MgO on nano-sized porous Si (pSi) dendrites obtained by etching Al–Si alloy for LIBs. The reversible specific capacity of pSi@MgO electrode is 969.4 mA h/g after 100 cycles at 100 mA/g between 0.01 and 1.5 V, and it presents the discharge specific capacities of 1253.0, 885.5, 642.4, 366.2, and 101.4 mA h/g at 100, 500, 1000, 2000, and 5000 mA/g, respectively. What is more, it delivers a high reversible capacity of 765.1 mA h/g even at 500 mA/g after 200 cycles. The performance improvement can be attributed to the protection of the MgO layer and built-in space of porous Si for volume expansion upon cycling. These results illustrate that ALD derived coating is a powerful strategy to enhance electrical properties of anode materials with huge volume change for lithium-ion batteries.

Introduction

With the development of portable electronic devices and electric cars, the lithium-ion batteries become the primary technology [1, 2]. In order to adapt the growing energy needs, high energy density and long-term cycling stability have become the major selection criteria for lithium-batteries electrode materials.

Some cathode and anode materials with high capacity including metal oxides (e.g., Fe_2O_3 and CuO), Li–Sn, Li–Ge, and Li–Si alloys provide superior performance compared to the traditional commercial graphite electrode (372 mA h/g) [3–7]. Among these materials, Si has been regarded as the most promising candidate material for a high theoretical specific capacity of 3579 mA h/g (corresponds to $Li_{15}Si_4$ at room temperature), lower operating potential (~0.2 V versus Li/Li^+), and abundance of Si resource on earth [8, 9, 10, 11]. Nonetheless, the application of Si anode faces some challenges, such as the ~300% volume expansion/shrinkage during the repeated lithium alloying/de-alloying processes which leads to pulverization and cracking of Si and rapid capacity decay, as well as worse performance [12, 13, 14]. Besides, solid electrolyte interphase films, produced by the decomposition of organic electrolyte, will be reformed on the freshly exposed silicon surface during volume change. The thicker SEI would lead to irreversible capacity loss, inferior-rate capacity, and low coulombic efficiency of Si-based anode [15, 16]. Moreover, the low electrical conductivity will inevitably cause poor kinetics and limit reaction rate, which makes it impossible for Si anode to obtain excellent electrochemical properties. Therefore, despite the unique advantages and an enormous potential of Si materials for high-performance lithium batteries, the above three major drawbacks seriously prevent the Si electrodes from its practical commercial application.

In order to solve the aforementioned problems, many approaches to improve the electrochemical properties of Si

https://doi.org/10.1557/jmr.2019.150 Published online by Cambridge University Press

© Materials Research Society 2019

electrodes have been studied, mainly by including minimizing the particle size [17, 18], coating Si with a second phase [19], and adopting new binders such as self-healing polymers and alginate [20, 21]. Meanwhile, various structures of Si have been synthesized such as porous structures [22], nanotubes [23], nanowires [24], and so on. For instance, Bao et al. [25] demonstrated a three-dimensional hierarchical structure of cyclized-PAN/Si/Ni through the plasma-enhanced chemical vapor deposition method and represented 1200 mA h/g after 100 cycles at 100 mA/g. Yi et al. [26] proposed a microsized Si–C material, which uses SiO as precursor. These methods all improve the cycle performance of silicon to some extent. Atomic layer deposition (ALD), as a novel strategy, can deposit relatively uniform thin films and the thickness of the coating can be controlled by adjusting the number of ALD cycles [27, 28]. Diverse studies have also illustrated that thin Al_2O_3 [29], TiO_2 [30–32], and TiN [33, 34, 35] passivation layers can increase both the structural and interfacial stabilities of Si-based composites. So far, ALD has not been applied to coat Si anodes with magnesium oxide.

In previous works, various Si anodes were synthesized by magnesiothermic reduction or other complicated processes [36, 37]. Here, we prepare porous Si anode by a simple approach of etching Al–Si alloy. Meanwhile, to find an ideal method to enhance the performance of Si anode, we use ALD to deposit the MgO coating layer on the nano-sized Si dendrites. The obtained pSi@MgO composite exhibits good electrochemical performance due to the following reasons: (i) The built-in space of porous Si can mitigate the volume expansion, (ii) the uniform MgO layer may decrease the contact between active materials and electrolyte, and (iii) the MgO layers deposited by ALD are more compact than other methods [38, 39, 40]. The most important thing is the thickness of MgO film could be digitally controlled by the adjustment of cycling numbers [41]. To date, the effect of MgO coating by ALD on Si anode performance has not been reported yet. It is of great significance to study the application of ALD in lithium-ion batteries.

In this work, the low-cost commercial Al–Si alloy was used as silicon precursor. Nano-sized porous Si dendrites were synthesized by a facile approach from etching the Al–Si alloy. Then, the thin MgO film was coated onto the nano-sized Si dendrites via ALD as the anode material for LIBs. As a result, the obtained pSi@MgO electrodes show good electrochemical performance by controlling the thickness of MgO.

Results and discussion

Figure 1 depicts the synthesis of pSi@MgO electrodes. In this work, the Si nanoparticles were obtained by etching Al–Si alloy. Then, the MgO layer was deposited on the Si nanoparticles by ALD method. The thickness of the MgO coating is highly sensitive in our work. It is a good illustration of the tremendous impact on the material properties of optimizing the thickness of MgO [42].

All samples were measured by X-ray power diffraction (XRD). As shown in Fig. 2(a), the Al–Si alloy exhibits the characteristic peaks of Al (2θ = 38.8°, 44.7°, 65.1°, and 78.2°) and one of the strongest peaks of silicon (2θ = 28.5°). And from Fig. 2(b), only five distinct diffraction peaks of Si at the 2θ values of 28.5°, 47.3°, 56.0°, 69.1°, and 76.4° were observed, which can be indexed to the (111), (220), (311), (400), and (331) crystal planes (JCPDS Card No. 27-1402), respectively. It indicates that after treatment with HCl and HF, the diffraction peaks of Al vanished and the porous Si dendrites exhibited a representative crystal structure. The patterns of pSi@MgO (2C), pSi@MgO (5C), and pSi@MgO (10C) are both exhibited in Fig. 2(b) for comparison. It can be seen that for pSi@MgO materials, no diffraction peaks corresponding to MgO have been found. This phenomenon may occur due to the following: (i) the MgO layer on the cathode electrode is an amorphous phase; (ii) the MgO layer is ultra-thin [43]. Furthermore, a broad bulge can be seen, suggesting that pSi with a high specific surface area has high activity and is easily oxidized even in an ambient atmosphere.

Scanning electron microscopy (SEM) was conducted to observe the surface morphology of different samples, as presented in Fig. 3. Figure 3(a) shows that the purchased Al–Si alloys are solid sphere shape with an average size of 3–5 μm. The structural evolution of Al–Si alloy at different etching times is observed in Figs. 3(b)–3(d). After etching process for 6 or 8 h, the solid sphere was transformed into porous Si dendrites, which were interconnected together highly. The alloy balls were broken into dendrites separately to some extent with a thickness of ~50 nm at 10 h etching. The Al–Si alloy treated by HCl and HF is shown in Figs. 3(e) and 3(f). HF was used to remove the metal oxides. The obtained samples exhibit a porous property [Fig. S1(a), in Supplementary material], which could be profitable to the intercalation of Li^+ and mitigate the change in the volume of Si upon cycling [44, 45, 46].

Figure 4 shows the typical images to better understand the morphology and constituent elements of the modified material: SEM, HRTEM, FFT diffraction pattern of pSi@MgO (10C) (a–c), and EDS elemental mapping data of pSi@MgO (50C) (d–f). In Fig. 4(a), the morphology of the porous Si dendrites is maintained and no obvious ultra-thin thickness of the MgO layer is observed. Evidently, transmission electron microscopy (TEM) observation of pSi@MgO (10C) indicates the existence of MgO coatings with a thickness of 2 nm in Fig. 4(b). It also reveals the poor crystallinity of MgO and well crystallized Si dendrites with a lattice fringe of 0.31 nm in (111) direction. To confirm the pore structure of pSi@MgO (10C), the N_2

https://doi.org/10.1557/jmr.2019.150 Published online by Cambridge University Press

© Materials Research Society 2019

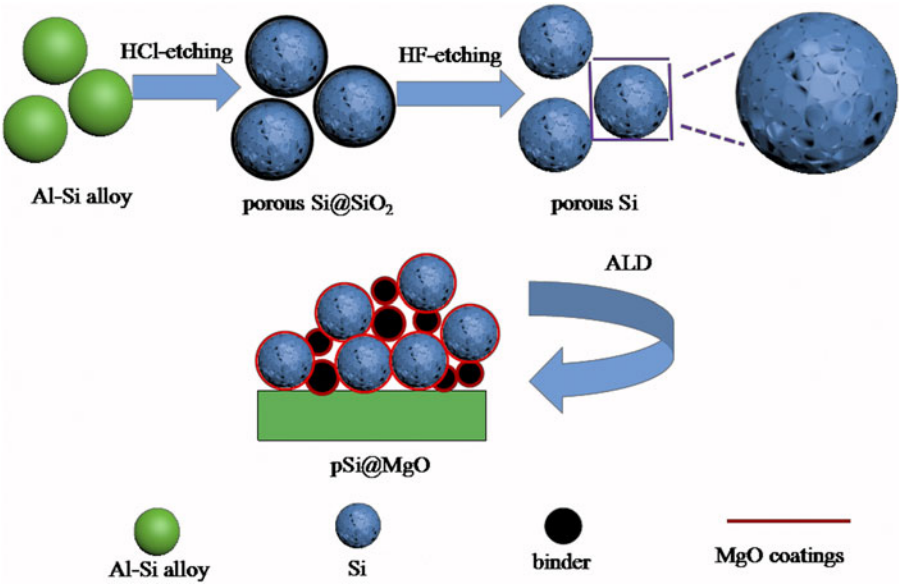


Figure 1: Synthesis process for pSi@MgO electrodes.

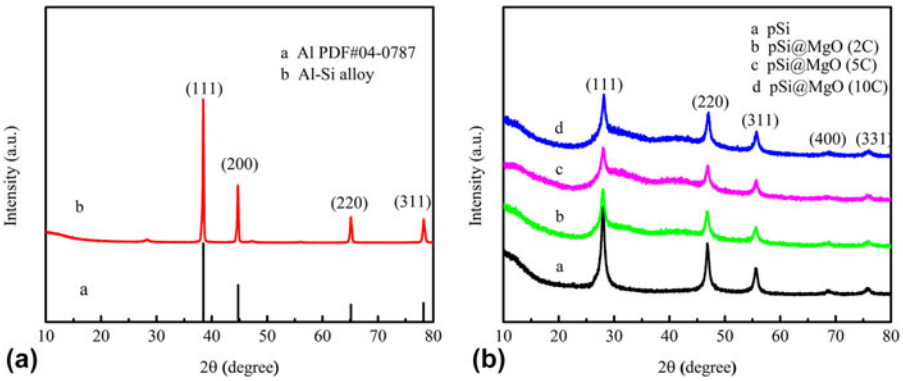


Figure 2: XRD patterns of (a) Al–Si alloy, (b) pSi, pSi@MgO (2C), pSi@MgO (5C), and pSi@MgO (10C).

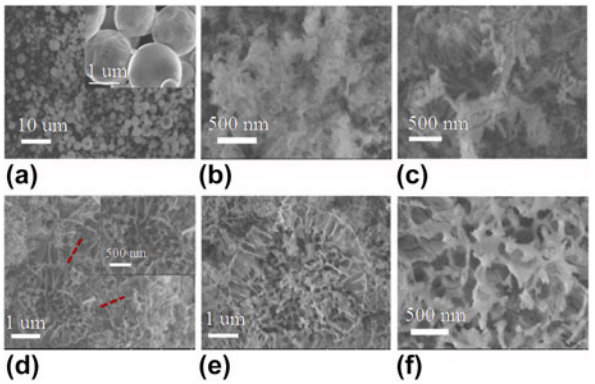


Figure 3: SEM images of Al–Si alloy at different etching times (a) 0 h, (b) 6 h, (c) 8 h, (d) 10 h, and (e, f) 10 h before treated by 2% HF 2 h.

adsorption/desorption measurement was carried out and the results (Fig. S1, in Supplementary material) show that the specific surface area and the pore size distribution were not changed significantly after ALD coating. Therefore, the MgO layer may prevent the contact of electrolyte and Si. In addition, it can relieve huge volume changes during the charge/discharge processes. In Fig. 4(c), the selected electron diffraction pattern of pSi@MgO (10C) demonstrates crystal Si anode. In Figs. 4(d)–4(f), elemental mapping of Si and Mg shows that these elements are evenly distributed across selected regions, indicating that MgO is uniformly covered on pSi.

The high resolution Si 2*p* spectrum of pSi and pSi@MgO (10C) composites is characterized by X-ray photoelectron spectroscopy (XPS), as presented in Fig. 5. As seen in Figs. 5(a) and 5(b), a 98-eV peak associated with the Si–Si bond represents monatomic silicon, and 102.5 eV corresponds to the SiO_x components ($x \leq 2$). It is due that Si nanoparticles having a high specific surface area can be easily oxidized even in the ambient atmosphere. We also found that the intensity of SiO_x peaks increased after ALD process because that the

https://doi.org/10.1557/jmr.2019.150 Published online by Cambridge University Press

© Materials Research Society 2019

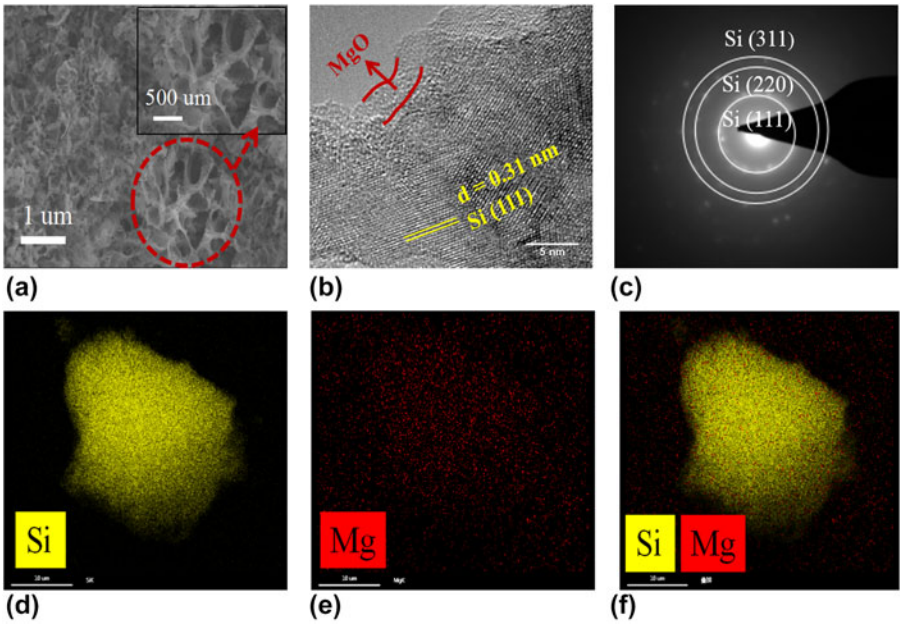


Figure 4: The typical images of the as-prepared materials: SEM, HRTEM, SAED pattern of pSi@MgO (10C) (a–c), and EDS mappings of Si, Mg, and overlay elemental mappings for Si and Mg in pSi@MgO (50C) (d–f).

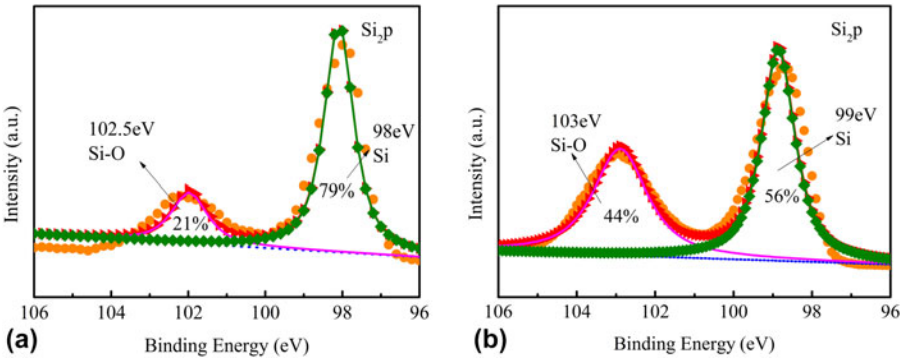


Figure 5: XPS spectra of Si_2p of (a) pSi and (b) pSi@MgO (10C).

oxidation of nano-sized Si becomes easily. In addition, the presence of SiO_x layers as a mesophase not only enhances the adhesive force of MgO on Si nanoparticles but also improves the electrochemical stability [47, 48].

Figures 6(a) and 6(b) show the cyclic voltammetry (CV) measurement of pSi and pSi@MgO (5C) electrode at 0.1 mV/s between 0.01 and 1.5 V. As presented in Fig. 6(a), a cathodic peak of 0.37 V is observed at the first scan and then disappeared in the subsequent scans, which may be caused by the SEI film formed on the electrode surface. In the remaining cathode scans, a reduction peak of 0.1 V is considered to be the formation of Li_xSi phase. During the process of oxidation, one main peak appeared at 0.5 V, which corresponds to the de-alloying reaction of the Li_xSi alloy to Si. Compared to Fig. 6(b), pSi@MgO (5C) electrode represents stronger cathodic and anodic peaks indicating the better capacity retention and high reversibility [49].

Figures 6(c) and 6(d) show the charge–discharge profiles of pSi and pSi@MgO (5C) electrodes at 100 mA/g within a voltage range of 0.01–1.5 V. During the first lithiation process, they exhibit a long and low plateau at 0.1 V while the plateau increased to 0.2 V in the later cycles. This indicates that the lithiation potential in amorphous Si is higher than that in crystal Si [50]. Compared with Fig. 6(d), the 10th and 20th charging and discharging curves of pSi@MgO (5C) are overlapped to a large extent, which means that the electrode has a good cycling performance. The initial discharge and charge specific capacities of pSi are 2378.8 and 1209.8 mA h/g, respectively. Meanwhile, the coulombic efficiency is only 50.86% because of the formation of SEI film and the irreversible lithium ion in the anode [51, 52]. In the 10th and 20th cycles, the discharge capacities decreased to 1117.2 and 962.5 mA h/g. The dramatic loss of capacity may be caused by the structural

https://doi.org/10.1557/jmr.2019.150 Published online by Cambridge University Press

© Materials Research Society 2019

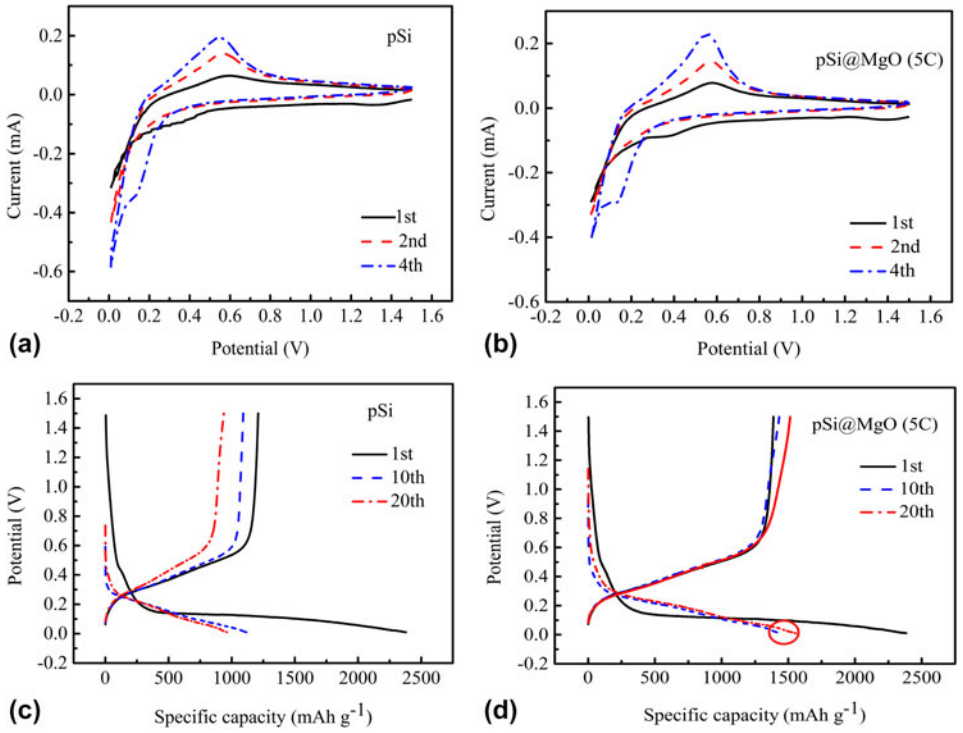


Figure 6: The CV curves of (a) pSi and (b) pSi@MgO (5C) in the 1st, 2nd, and 4th cycles and the charge–discharge profiles of (c) pSi and (d) pSi@MgO (5C) in the 1st, 10th, and 20th cycles at 100 mA h/g.

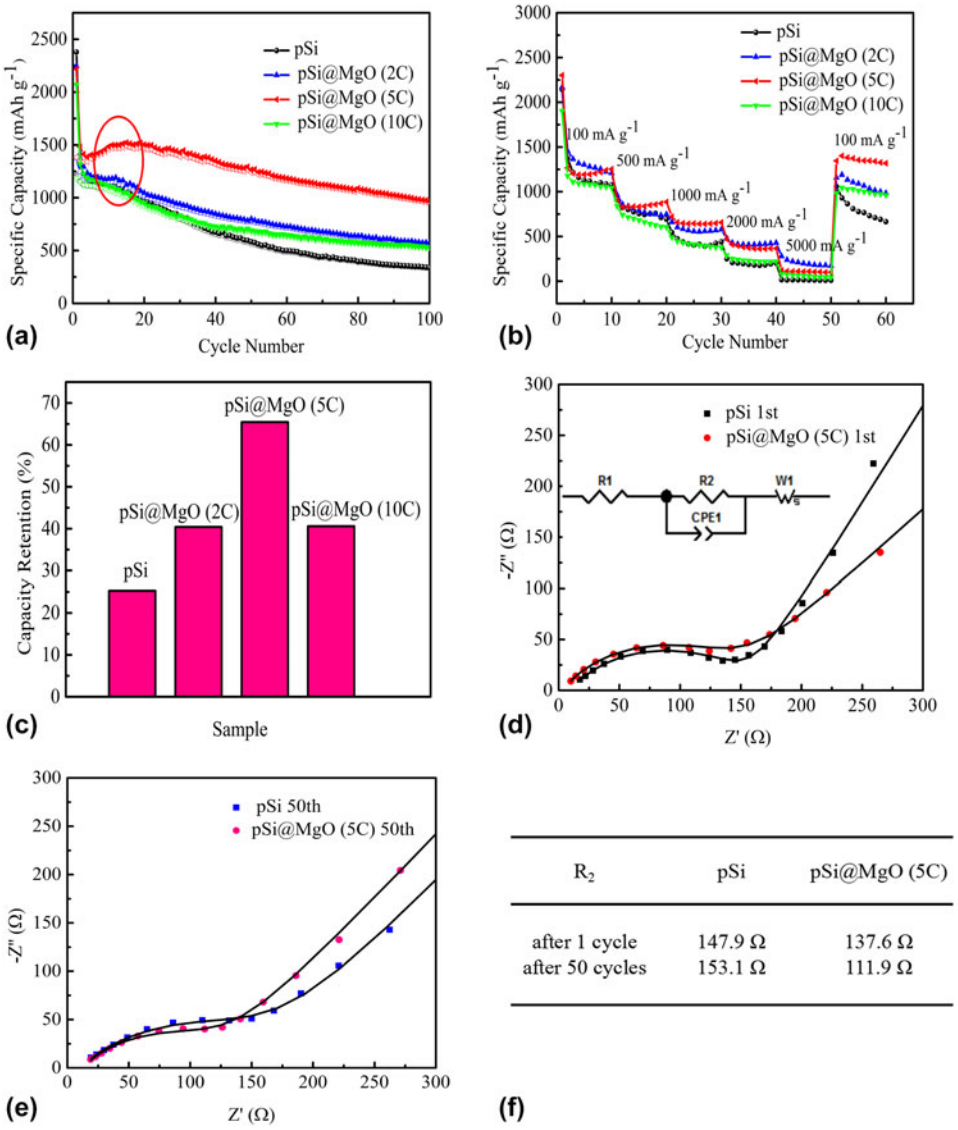
degradation. Comparatively, the pSi@MgO (5C) delivers an initial discharge and charge specific capacities of 2218.3 and 1384.7 mA h/g with a coulombic efficiency of 62.42% as shown in Fig. 6(d). This increase is associated with the protection of MgO. The presence of MgO coatings prevents the surface of pSi from being exposed to the electrolyte, reducing side reactions and forming a stable SEI film [53]. In addition, the porous structure and MgO layer are capable of accommodating volume expansion. Then, the specific discharge capacity increases to 1517.8 mA h/g at the 20th cycle due to the protection of MgO layer.

The cycling performance of various pSi@MgO composite electrodes is shown in Fig. 7(a) under a current density of 100 mA/g. It is obvious that the capacity of pSi decreases energetically. After coating MgO by ALD method, the performance exhibits a certain improvement particularly for the pSi@MgO (5C). This is because the volume change of the modified material is somewhat relieved. As with the result of the charge–discharge profiles, the specific capacity increased in the initial cycles. As with the result of the charge–discharge profiles, the specific capacity increased during the first 20 cycles. Such increase may be attributed to the following reasons: the Si inside the particles is not activated or fully discharged due to the longer diffusion distance of lithium ions. With deeper diffusion of Li^+, the inside Si will be activated upon initial cycles which causing more active sites to be exposed and resulting in increased capacity. However, the specific capacity of pSi@MgO (10C) electrodes decays faster in the initial 50 cycles. The loss may be caused by the lower electrical conductivity of poor-crystallized MgO film. Figure 7(b) exhibits the rate capacity of pSi, pSi@MgO (2C), pSi@MgO (5C), and pSi@MgO (10C) at various current densities. The pSi delivers reversible specific capacities of 1076.4, 693.9, 440.2, 201.9, and 11.1 mA h/g at 100, 500, 1000, 2000, and 5000 mA/g, respectively, and its capacity only reaches 665.4 mA h/g as the current density is restored to 100 mA/g after 50 cycles. As the current density is gradually increased, the specific capacity of the sample is decreasing. This indicates that the large current density causes serious damage to the electrode structure and degrades its electrochemical properties. After 50 cycles, the electrode capacity is greatly improved when the current density back to an initial value of 100 mA/g. It shows that the structure of the electrode has a certain stability and does not completely destroyed at a large current density. It is obvious that a thin MgO layer could improve the rate performance. Especially for pSi@MgO (5C), after 50 cycles, it can recover to 1319 mA h/g at 100 mA/g. Figure 7(c) shows the capacity retention of pSi, pSi@MgO (2C), pSi@MgO (5C), and pSi@MgO (10C) after 100 cycles. Obviously, the pSi@MgO (5C) presents the better performance.

For a better study of the reaction kinetics of the electrode surface, EIS measurement of the various electrodes is

https://doi.org/10.1557/jmr.2019.150 Published online by Cambridge University Press

© Materials Research Society 2019



R_2	pSi	pSi@MgO (5C)
after 1 cycle	147.9 Ω	137.6 Ω
after 50 cycles	153.1 Ω	111.9 Ω

(f)

Figure 7: (a) Cycling performance at 100 mA/g, (b) rate capability and (c) specific capacity retention of pSi, pSi@MgO (2C), pSi@MgO (5C), and pSi@MgO (10C) after 100 cycles. (d, e) EIS and equivalent circuit of pSi and pSi@MgO (5C). (f) The fitted parameters of charge-transfer resistance (R_2).

performed. Figures 7(d) and 7(e) show the Nyquist impedance spectra and the equivalent circuit diagram of the pSi and pSi@MgO (5C). In this equivalent circuit, R_1 (a semi-circular intercept on the real axis) characterizes the resistance of electrolyte. R_2 (semicircles in middle frequency range) indicates resistance of the Li^+ transfer at interface between the electrode and the electrolyte. W_1 (inclined line in low frequency range) is the Warburg impedance that diffuses to the electrode for Li-ion. It is noted that the R_1 of pSi and pSi@MgO (5C) are 8.803 Ω and 2.888 Ω after 1 cycle, respectively. The lower resistance of pSi@MgO (5C) may be attributed to the stable SEI formation. The R_2 values are displayed in Fig. 7(f). It is evident that the R_2 of the pSi@MgO (5C) is lower than pSi, indicating that the diffusion and transfer ability of lithium ions is faster.

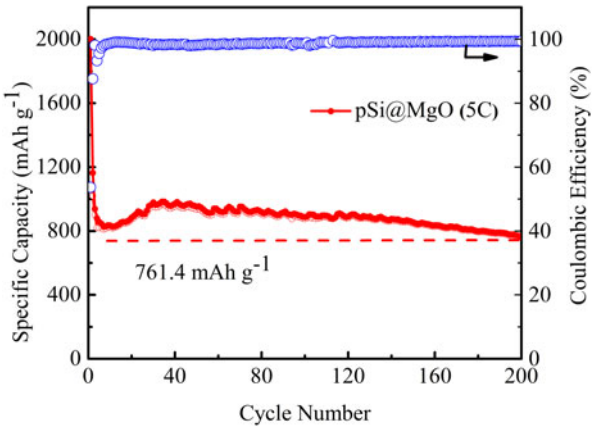


Figure 8: Cycling performance of pSi@MgO (5C) at a current density of 500 mA/g.

https://doi.org/10.1557/jmr.2019.150 Published online by Cambridge University Press

© Materials Research Society 2019

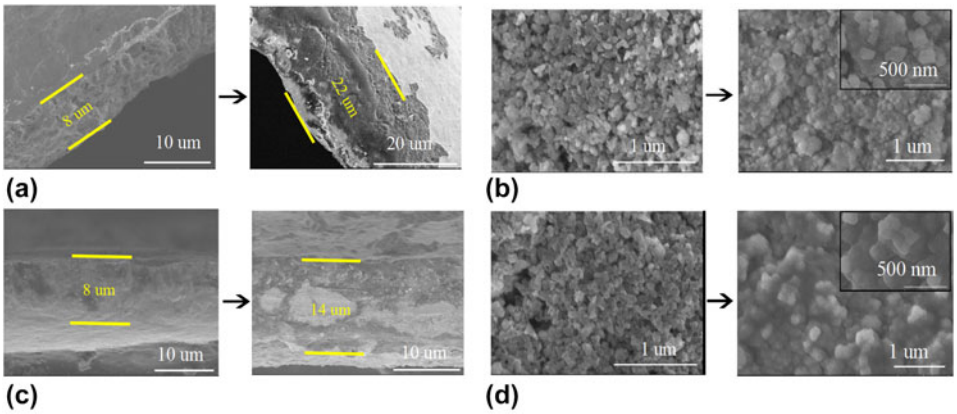


Figure 9: Cross-sectional and SEM images of the (a, b) pSi and (c, d) pSi@MgO (5C) before and after 50 cycling.

After 50 cycles, the R_2 for the pSi@MgO (5C) electrode decreases from 137.6 to 111.9 Ω, which is accord with the excellent electrochemical performance.

We perform a long-term cycling test on pSi@MgO (5C) electrodes at a current density of 500 mA/g. It can be seen from Fig. 8 that pSi@MgO (5C) demonstrates favorable cycle stability, and a high reversible capacity of 765.1 mA h/g is remained after 200 cycles. The obvious problem of silicon-based materials is volume expansion/shrinkage upon cycling. In order to study the changes of Si anode materials during cycling, the SEM was used to characterize the volume expansion in Fig. 9. Figures 9(a) and 9(b) indicate that the thickness of the pSi composite electrode increases from 8 um to 22 um, and some Si particles crack after 50 cycles. In contrast, the thickness of the pSi@MgO (5C) increases from 8 um to 14 um, and the Si articles still exist after 50 cycles. This provides a further proof for the stable electrochemical properties of the pSi@MgO (5C) electrode as shown in Fig. 7.

Conclusion

In this paper, the pSi@MgO composites were successfully synthesized via an ALD method. The thickness of the MgO coating is determined by the number of ALD cycles and the electrochemical tests show that the performance of pSi@MgO (5C) is better. The modified electrode displays prominent cycling performance and rate capability due to the unique structure, including porous Si and MgO layer. The pSi@MgO (5C) electrode delivers a high coulombic efficiency of 98.57% and a reversible capacity of 969.4 mA h/g after 100 cycles. Moreover, it still has 765.1 mA h/g at 500 mA/g after 200 cycles. The cross-section SEM image after 50 cycles shows that the increase in the thickness of pSi@MgO (5C) was smaller than pSi. Therefore, a uniform MgO layer deposited by ALD could alleviate the huge volume change during the process of charging and discharging. It is also found that the anode performance is sensitive to the thickness of MgO layer, and the thicker layer with lower electrode performance may originate from the resistance of ion transmission. Today, surface modification by ALD, including coating electrodes or active materials, has been widely used. To a certain extent, our work provides insights into application and understanding of ALD strategy in next generation rechargeable batteries.

Experimental

Preparation of porous Si dendrites

The Al–Si alloy (Al:Si = 90:10 wt%, Titd Metal Materials Co., Ltd., Changsha, China) as the silicon source was used to prepare nano-sized Si dendrites anode materials via chemical-etching. First, 4 g of Al–Si powders were added into 44 mL of deionized water and 10 mL of HCl (38 wt%) solution. The obtained solution was continuously stirred for 10 h to remove Al element. Afterward, the obtained product was centrifuged and then treated with 2% HF for 2 h to dispose of oxides on the silicon surface. Finally, the materials were cleaned by deionized water and ethanol and dried for one night in a vacuum at 60 °C.

Preparation of pSi@MgO composites

We use the ALD R200 Advanced system (Picosun, Finland Picosun, Finland) to deposit MgO [54]. The Mg precursor was bis-encyclopedic magnesium, and H_2O was used as oxidizer. The reaction temperature was set as 250 °C. A typical cycle was carried out with the following four steps: (i) pulsing bis-cyclopentadienyl magnesium into reaction chamber for 0.1 s; (ii) eliminating the unconsumed bis-cyclopentadienyl magnesium and any by-products for 4 s; (iii) pulsing H_2O into reaction chamber for 0.1 s; (iv) eliminating by-products and the unconsumed H_2O for 4 s. MgO was deposited on the porous silicon dendrites with different cycles as 2, 5, and 10, which were named as pSi@MgO (2C), pSi@MgO (5C), and pSi@MgO (10C).

https://doi.org/10.1557/jmr.2019.150 Published online by Cambridge University Press

© Materials Research Society 2019

Material characterization

X-ray power diffraction (XRD; D8 Advance of Bruker, Bruker Corp., Beijing, China) measurements were used to investigate the crystalline phases of samples of Cu K_α radiation (γ = 1.54145 Å) in a 2θ range of 10°–80°. The scanning electron microscopy (SEM; SU8010, Hitachi, Ltd., Tokyo, Japan) and transmission electron microscopy (TEM; TecnaiG2 F30, FEI Company, Hillsboro, Oregon) were performed to observe the surface morphology and nanostructure of samples. The chemical composition and relative proportion about the electrode material were obtained by surface-sensitive X-ray photoelectron spectroscopy (XPS; VG ESCALAB MK II, VG Scienta, St Leonards-on-Sea, U.K).

Electrochemical measurements

For the fabrication of working electrodes, 70 wt% porous silicon, 20 wt% carbon black, and 10 wt% carboxyl methyl cellulose were mixed together. Then apply the slurry to the Cu foil and dry. The electrolyte was comprised of 1 M LiPF6 in a solvent mixture of ethylene carbonate (EC)/dimethyl carbonate (DMC)/fluoroethylene carbonate (FEC) (1:1:1 in volume). The lithium foil was employed as the counter electrode for the assembly of CR2032-type coin cells in an argon-filled glove box, where it contains oxygen less than 0.1 ppm. To ensure the enough soakage, the batteries were aged for 12 h before the electrochemical measurements. The cells were tested using a Land battery tester (LANHE CT2001A, Wuhan LAND electronics Co., Ltd., Wuhan, China) within 0.01–1.5 V (versus Li/Li^+). CV was conducted between the voltage of 0.01 and 1.5 V (versus Li/Li^+). The electrochemical impedance spectroscopy (EIS) measurements were tested between 100 kHz and 0.01 Hz.

Acknowledgments

This research was supported by the National Natural Science Foundation of China (51572194 and 51672189), the Key Projects of Tianjin Municipal Natural Science Foundation of China (14JCZDJC32200), and Tianjin Science and Technology Project (18PTZWHZ00020).

Supplementary material

To view supplementary material for this article, please visit https://doi.org/10.1557/jmr.2019.150.

References

1. **Y. Ding, Z.P. Cano, A. Yu, J. Lu, and Z. Chen**: Automotive Li-ion batteries: Current status and future perspectives. *Electrochem. Energy Rev.* **2**, 1 (2019).
2. **K. Yao, J.P. Zheng, and Z. Liang**: Binder-free freestanding flexible Si nanoparticle–multi-walled carbon nanotube composite paper anodes for high energy Li-ion batteries. *J. Mater. Res.* **33**, 482 (2018).
3. **W-M. Zhang, J-S. Hu, Y-G. Guo, S-F. Zheng, L-S. Zhong, W-G. Song, and L-J. Wan**: Tin-nanoparticles encapsulated in elastic hollow carbon spheres for high-performance anode material in lithium-ion batteries. *Adv. Mater.* **20**, 1160 (2008).
4. **Y. Liang, H. Tian, J. Repac, S-C. Liou, J. Chen, W. Han, C. Wang, and S. Ehrman**: Colloidal spray pyrolysis: A new fabrication technology for nanostructured energy storage materials. *Energy Storage Mater.* **13**, 8 (2018).
5. **H. Tian, Y. Liang, J. Repac, S. Zhang, C. Luo, S-C. Liou, G. Wang, S.H. Ehrman, and W. Han**: Rational design of core–shell-structured particles by a one-step and template-free process for high-performance lithium/sodium-ion batteries. *J. Phys. Chem. C* **122**, 22232 (2018).
6. **W-J. Zhang**: A review of the electrochemical performance of alloy anodes for lithium-ion batteries. *J. Power Sources* **196**, 13 (2011).
7. **M.N. Obrovac and V.L. Chevrier**: Alloy negative electrodes for Li-ion batteries. *Chem. Rev.* **114**, 11444 (2014).
8. **A. Magasinski, P. Dixon, B. Hertzberg, A. Kvit, J. Ayala, and G. Yushin**: High-performance lithium-ion anodes using a hierarchical bottom-up approach. *Nat. Mater.* **9**, 353 (2010).
9. **H. Wu and Y. Cui**: Designing nanostructured Si anodes for high energy lithium ion batteries. *Nano Today* **7**, 414 (2012).
10. **B. Liang, Y. Liu, and Y. Xu**: Silicon-based materials as high capacity anodes for next generation lithium ion batteries. *J. Power Sources* **267**, 469 (2014).
11. **H. Tian, F. Xin, X. Wang, W. He, and W. Han**: High capacity group-IV elements (Si, Ge, Sn) based anodes for lithium-ion batteries. *J. Materiomics* **1**, 153 (2015).
12. **K. Mishra, X-C. Liu, M. Geppert, J.J. Wu, J-T. Li, L. Huang, S-G. Sun, X-D. Zhou, and F-S. Ke**: Submicro-sized Si–Ge solid solutions with high capacity and long cyclability for lithium-ion batteries. *J. Mater. Res.* **33**, 1553 (2018).
13. **I. Kovalenko, B. Zdyrko, A. Magasinski, B. Hertzberg, Z. Milicev, R. Burtovyy, I. Luzinov, and G. Yushin**: A major constituent of brown algae for use in high-capacity Li-ion batteries. *Science* **334**, 75 (2011).
14. **D.S. Jung, M.H. Ryou, Y.J. Sung, S.B. Park, and J.W. Choi**: Recycling rice husks for high-capacity lithium battery anodes. *Proc. Natl. Acad. Sci. U. S. A.* **110**, 12229 (2013).
15. **Y. Zhao, L. Zheng, H. Wu, H. Chen, L. Su, L. Wang, Y. Wang, and M. Ren**: Co_2SiO_4/SiO_2/RGO nanosheets: Boosting the lithium storage capability of tetravalent Si by using highly-dispersed Co element. *Electrochim. Acta* **282**, 609 (2018).
16. **F. Dou, L. Shi, G. Chen, and D. Zhang**: Silicon/carbon composite anode materials for lithium-ion batteries. *Electrochem. Energy Rev.* **2**, 149 (2019).
17. **B. Zhu, Y. Jin, Y. Tan, L. Zong, Y. Hu, L. Chen, Y. Chen, Q. Zhang, and J. Zhu**: Scalable production of Si nanoparticles

https://doi.org/10.1557/jmr.2019.150 Published online by Cambridge University Press

© Materials Research Society 2019

directly from low grade sources for lithium-ion battery anode. *Nano Lett.* **15**, 5750 (2015).

18. **H. Song, H.X. Wang, Z. Lin, X. Jiang, L. Yu, J. Xu, Z. Yu, X. Zhang, Y. Liu, P. He, L. Pan, Y. Shi, H. Zhou, and K. Chen**: Highly connected silicon-copper alloy mixture nanotubes as high-rate and durable anode materials for lithium-ion batteries. *Adv. Funct. Mater.* **26**, 524 (2016).
19. **Z. Lu, N. Liu, H.W. Lee, J. Zhao, W. Li, Y. Li, and Y. Cui**: Nonfilling carbon coating of porous silicon micrometer-sized particles for high-performance lithium battery anodes. *ACS Nano* **9**, 2540 (2015).
20. **C. Wang, H. Wu, Z. Chen, M.T. McDowell, Y. Cui, and Z. Bao**: Self-healing chemistry enables the stable operation of silicon microparticle anodes for high-energy lithium-ion batteries. *Nat. Chem.* **5**, 1042 (2013).
21. **H. Zhao, A. Du, M. Ling, V. Battaglia, and G. Liu**: Conductive polymer binder for nano-silicon/graphite composite electrode in lithium-ion batteries towards a practical application. *Electrochim. Acta* **209**, 159 (2016).
22. **H. Tian, X. Tan, F. Xin, C. Wang, and W. Han**: Micro-sized nano-porous Si/C anodes for lithium ion batteries. *Nano Energy* **11**, 490 (2015).
23. **M.H. Park, M.G. Kim, J. Joo, K. Kim, J. Kim, S. Ahn, Y. Cui, and J. Cho**: Silicon nanotube battery anodes. *Nano Lett.* **9**, 3844 (2009).
24. **N. Liu, L.B. Hu, M.T. McDowell, A. Jackson, and Y. Cui**: Prelithiated silicon nanowires as an anode for lithium ion batteries. *ACS Nano* **5**, 6487 (2011).
25. **W. Bao, J. Wang, S. Chen, W. Li, Y. Su, F. Wu, G. Tan, and J. Lu**: A three-dimensional hierarchical structure of cyclized-PAN/Si/Ni for mechanically stable silicon anodes. *J. Mater. Chem. A* **5**, 24667 (2017).
26. **R. Yi, F. Dai, M.L. Gordin, S. Chen, and D. Wang**: Micro-sized Si–C composite with interconnected nanoscale building blocks as high-performance anodes for practical application in lithium-ion batteries. *Adv. Energy Mater.* **3**, 295 (2013).
27. **D. Zhang, Y. Xu, G. Feng, Y-R. Huang, and D. Lee**: Comparing sintering and atomic layer deposition as methods to mechanically reinforce nanocolloidal crystals. *J. Mater. Res.* **30**, 3717 (2015).
28. **C. Luo, H. Zhu, W. Luo, F. Shen, X. Fan, J. Dai, Y. Liang, C. Wang, and L. Hu**: Atomic-layer-deposition functionalized carbonized mesoporous wood fiber for high sulfur loading lithium sulfur batteries. *ACS Appl. Mater. Interfaces* **9**, 14801 (2017).
29. **G. Hwang, H. Park, T. Bok, S. Choi, S. Lee, I. Hwang, N.S. Choi, K. Seo, and S. Park**: A high-performance nanoporous Si/Al_2O_3 foam lithium-ion battery anode fabricated by selective chemical etching of the Al–Si alloy and subsequent thermal oxidation. *Chem. Commun.* **51**, 4429 (2015).
30. **J. Wang, Y. Zhou, Y. Hu, R. O'Hayre, and Z. Shao**: Facile synthesis of nanocrystalline TiO_2 mesoporous microspheres for lithium-ion batteries. *J. Phys. Chem. C* **115**, 2529 (2011).
31. **Z. Hong, M. Wei, T. Lan, L. Jiang, and G. Cao**: Additive-free synthesis of unique TiO_2 mesocrystals with enhanced lithium-ion intercalation properties. *Energy Environ. Sci.* **5**, 5408 (2012).
32. **N.D. Petkovich, S.G. Rudisill, B.E. Wilson, A. Mukherjee, and A. Stein**: Control of TiO_2 grain size and positioning in three-dimensionally ordered macroporous TiO_2/C composite anodes for lithium ion batteries. *Inorg. Chem.* **53**, 1100 (2014).
33. **N. Savvides and B. Window**: Electrical transport, optical properties, and structure of TiN films synthesized by low-energy ion assisted deposition. *J. Appl. Phys.* **64**, 225 (1988).
34. **S. Dong, X. Chen, L. Gu, X. Zhou, L. Li, Z. Liu, P. Han, H. Xu, J. Yao, H. Wang, X. Zhang, C. Shang, G. Cui, and L. Chen**: One dimensional MnO_2/titanium nitride nanotube coaxial arrays for high performance electrochemical capacitive energy storage. *Energy Environ. Sci.* **4**, 3502 (2011).
35. **A. Kohandehghan, P. Kalisvaart, K. Cui, M. Kupsta, E. Memarzadeh, and D. Mitlin**: Silicon nanowire lithium-ion battery anodes with ALD deposited TiN coatings demonstrate a major improvement in cycling performance. *J. Mater. Chem. A* **1**, 12850 (2013).
36. **T. Bok, S. Choi, J. Lee, and S. Park**: Effective strategies for improving the electrochemical properties of highly porous Si foam anodes in lithium-ion batteries. *J. Mater. Chem. A* **2**, 14195 (2014).
37. **N. Liu, Z. Lu, J. Zhao, M.T. McDowell, H.W. Lee, W. Zhao, and Y. Cui**: A pomegranate-inspired nanoscale design for large-volume-change lithium battery anodes. *Nat. Nanotechnol.* **9**, 187 (2014).
38. **L.A. Riley, S. Van Atta, A.S. Cavanagh, Y. Yan, S.M. George, P. Liu, A.C. Dillon, and S-H. Lee**: Electrochemical effects of ALD surface modification on combustion synthesized $LiNi_{1/3}Mn_{1/3}Co_{1/3}O_2$ as a layered-cathode material. *J. Power Sources* **196**, 3317 (2011).
39. **I.D. Scott, Y.S. Jung, A.S. Cavanagh, Y. Yan, A.C. Dillon, S.M. George, and S.H. Lee**: Ultrathin coatings on nano-$LiCoO_2$ for Li-ion vehicular applications. *Nano Lett.* **11**, 414 (2011).
40. **X. Li, J. Liu, M.N. Banis, A. Lushington, R. Li, M. Cai, and X. Sun**: Atomic layer deposition of solid-state electrolyte coated cathode materials with superior high-voltage cycling behavior for lithium ion battery application. *Energy Environ. Sci.* **7**, 768 (2014).
41. **X. Wang, Z. Guo, Y. Gao, and J. Wang**: Atomic layer deposition of vanadium oxide thin films from tetrakis(dimethylamino) vanadium precursor. *J. Mater. Res.* **32**, 37 (2016).
42. **Y. Bai, D. Yan, C. Yu, L. Cao, C. Wang, J. Zhang, H. Zhu, Y-S. Hu, S. Dai, J. Lu, and W. Zhang**: Core–shell $Si@TiO_2$ nanosphere anode by atomic layer deposition for Li-ion batteries. *J. Power Sources* **308**, 75 (2016).
43. **H. Kou, X. Li, H. Shan, L. Fan, B. Yan, and D. Li**: An optimized Al_2O_3 layer for enhancing the anode performance of $NiCo_2O_4$ nanosheets for sodium-ion batteries. *J. Mater. Chem. A* **5**, 17881 (2017).

https://doi.org/10.1557/jmr.2019.150 Published online by Cambridge University Press

© Materials Research Society 2019

44. **X. Li, Q. Chen, I. McCue, J. Snyder, P. Crozier, J. Erlebacher, and K. Sieradzki**: Dealloying of noble-metal alloy nanoparticles. *Nano Lett.* **14**, 2569 (2014).
45. **J. Feng, Z. Zhang, L. Li, J. Yang, S. Xiong, and Y. Qian**: Ether-based nonflammable electrolyte for room temperature sodium battery. *J. Power Sources* **284**, 222 (2015).
46. **J.S. Kim, W. Pfleging, R. Kohler, H.J. Seifert, T.Y. Kim, D. Byun, H-G. Jung, W. Choi, and J.K. Lee**: Three-dimensional silicon/carbon core–shell electrode as an anode material for lithium-ion batteries. *J. Power Sources* **279**, 13 (2015).
47. **X. Xin, X. Zhou, F. Wang, X. Yao, X. Xu, Y. Zhu, and Z. Liu**: A 3D porous architecture of Si/graphene nanocomposite as high-performance anode materials for Li-ion batteries. *J. Mater. Chem.* **22**, 7724 (2012).
48. **X. Zhou, K. Han, H. Jiang, Z. Liu, Z. Zhang, H. Ye, and Y. Liu**: High-rate and long-cycle silicon/porous nitrogen-doped carbon anode via a low-cost facile pre-template-coating approach for Li-ion batteries. *Electrochim. Acta* **245**, 14 (2017).
49. **X. Sun, W. Si, X. Liu, J. Deng, L. Xi, L. Liu, C. Yan, and O.G. Schmidt**: Multifunctional Ni/NiO hybrid nanomembranes as anode materials for high-rate Li-ion batteries. *Nano Energy* **9**, 168 (2014).
50. **Y. Zhou, H. Guo, G. Yan, Z. Wang, X. Li, Z. Yang, A. Zheng, and J. Wang**: Fluidized bed reaction towards crystalline embedded amorphous Si anode with much enhanced cycling stability. *Chem. Commun.* **54**, 3755 (2018).
51. **Y. Qi, C. Zhang, S. Liu, Y. Zong, and Y. Men**: Room-temperature synthesis of ZnO@GO nanocomposites as anode for lithium-ion batteries. *J. Mater. Res.* **33**, 1506 (2018).
52. **K.S. Chan, M.A. Miller, W. Liang, C. Ellis-Terrell, and C.K. Chan**: First principles and experimental studies of empty Si_{46} as anode materials for Li-ion batteries. *J. Mater. Res.* **31**, 3657 (2016).
53. **J. Lu, Z. Chen, F. Pan, Y. Cui, and K. Amine**: High-performance anode materials for rechargeable lithium-ion batteries. *Electrochem. Energy Rev.* **1**, 35 (2018).
54. **X. Li, J. Liu, X. Meng, Y. Tang, M.N. Banis, J. Yang, Y. Hu, R. Li, M. Cai, and X. Sun**: Significant impact on cathode performance of lithium-ion batteries by precisely controlled metal oxide nanocoatings via atomic layer deposition. *J. Power Sources* **247**, 57 (2014).

https://doi.org/10.1557/jmr.2019.150 Published online by Cambridge University Press

© Materials Research Society 2019